

Imaging fine structures of the human trabecular meshwork *in vivo* using a custom design gonioscopic lens and OCT gonioscopy

ALESSANDRA CARMICHAEL-MARTINS,^{*}  THOMAS J. GAST, BRETT J. KING, BRITTANY R. WALKER, MARCELINA SOBCZAK,  AND STEPHEN A. BURNS 

School of Optometry, Indiana University, Bloomington, Indiana 47401, USA

^{*}alecarmi@iu.edu

Abstract: The trabecular meshwork (TM), located within the iridocorneal angle, is a target for many glaucoma treatments aimed at controlling intraocular pressure. However, structural variations between individuals are poorly understood. We propose a newly designed gonioscopic lens optimized for high-resolution imaging to image fine structures of the human TM *in vivo*. The body of the new lens is index-matched to the human cornea and includes a choice of two gonioscopic mirrors (59° and 63°) and matching air-spaced doublets placed on the anterior surface of the gonioscopic lens. The new design allows a diffraction-limited image plane at the iridocorneal angle structures. The gonioscopic lens design was built and then placed on the subject's eyes coupled to the cornea with gonioscopy and a 3D adjustable mount. Images were obtained using a commercially available OCT device (Heidelberg Spectralis). The optical resolution was measured in a model eye as 40.32 and 45.25 μm respectively for each mirror angle. In humans, dense OCT scans with minimum spacing oriented tangential to the iris and ICA were performed on 7 healthy subjects (23–73 yrs). The TM was successfully imaged in all subjects. The custom gonioscopic lens improved the contrast of the uveoscleral meshwork structures and corneoscleral meshwork revealing limbus parallel striations, not visible with previous gonioscopic lens designs. Transverse OCT images were constructed along the segmentation line, providing an enface image of the TM structures including corneoscleral beams, previously only imaged *in vivo* using custom adaptive optics systems.

© 2023 Optica Publishing Group under the terms of the [Optica Open Access Publishing Agreement](#)

1. Introduction

Glaucoma is an optic neuropathy characterized by progressive structural and functional damage affecting approximately 64.3 million individuals worldwide [1,2]. It is a leading cause of irreversible vision loss and blindness in the world [1–4]. While glaucoma's etiology remains poorly understood, the factors contributing to damage are thought to include biomechanical changes associated with the interaction of elevated intraocular pressure (IOP) [5,6], cerebrospinal fluid pressure, and ocular hemodynamics. IOP is currently the only modifiable risk factor for glaucoma even though the correlation between elevated IOP and progressive glaucomatous damage is not high [7]. Most strategies to delay or avoid vision loss in glaucoma patients, even those with normal IOP, are targeted towards lowering IOP.

The IOP represents an equilibrium between aqueous humor inflow and outflow. The outflow is primarily through the anterior segment of the eye, through the trabecular meshwork (TM), the major outflow pathway. The TM is a layered sieve-like structure lying at the junction of the iris and cornea, known as the iridocorneal angle or ICA. Aqueous fluid, which is pumped into the eye by the ciliary body epithelium, drains through the TM then crosses the juxtacanalicular tissue into Schlemm's canal (SC), and from there continues into the episcleral aqueous veins. Anatomically, the TM is divided into three sections: the most proximal (adjacent to the iris) is the uveal

meshwork; the middle is the corneoscleral meshwork, and the most distal is the juxtacanalicular tissue, lying adjacent to SC [8]. A major cause of elevated IOP is not the overproduction of aqueous humor, but an increased resistance to outflow through the TM, thought to be in the juxtacanalicular area [8–11], as well as changes to the extracellular matrix of the TM [12–16]. This resistance is thought to be related to a higher molecular density of the glycosaminoglycans with age and/or an increase of fibrous-granular material in the TM [17].

Unfortunately, most *in vivo* studies of the TM are limited as light returning from the TM at high angles is totally internally reflected at the corneal surface [18]. To overcome this restriction, a specialized lens coupled to the cornea, known as a gonioscopic lens or goniolens, is used to reduce the refractive index difference between the cornea and air. A typical goniolens consists of a PMMA conical frustum body with one or more interior flat mirrors positioned at angles of 59° to 64°, and a back curved surface with a radius similar to that of the cornea. The lens is placed in direct contact with the cornea, optically mating the lens to the cornea using a viscous fluid, such as goniogel. Typically, the ICA, including the TM is visualized using a slit lamp, allowing only 2D images of the region at low resolution.

Our group has shown that an Adaptive Optics Scanning Laser Ophthalmoscope (AOSLO) coupled with a modified gonioscopic lens can be used to image the TM *in vivo* achieving cellular-level resolution enface images of these tissue structures [19]. Others have obtained full 3D images of the ICA using anterior segment Optical Coherence Tomography (OCT), typically at lower resolution laterally [20–28], by imaging through the limbus of the eye. This imaging modality is limited by the scattering of light from the overlying scleral tissue. Recently a custom anterior segment OCT was developed achieving interesting images of SC and collector channels in a cadaver eye [29]. Another OCT system has also been developed [30] to image this region providing increased depth information and capturing a 360° view of the angle, using a customized goniolens, with an optimal resolution of 24 μm . These studies used highly customized OCT systems which come at a high cost and are not yet suitable for the clinical setting. We have recently shown that a combination of these imaging modalities is also possible by using a widely available OCT imaging system (Heidelberg Spectralis) with a minimally modified gonioscopic lens, to image the ICA structures *in vivo* through the transparent cornea [18]. This approach would allow for more widespread imaging of the ICA in the clinical setting.

In the current paper, we propose a new gonioscopic lens optimized to improve the resolution of our OCT Gonioscopy with the commercial OCT device. Optical ray tracing software (Zemax Optic Studio) is used to analyze and reduce the main source of aberrations in gonioscopic imaging to produce diffraction-limited performance over a 1mm^2 area. The new goniolens fabrication process is described and tested, achieving higher optical lateral resolution than any other system, to our knowledge, without adaptive optics. Gonioscopic OCT images of healthy subjects show cellular structures within the TM, such as lamellar-like striations similar to the collagenous layers forming the TM as seen in histology [10]. These structures have only been seen previously *in vivo* using custom Adaptive Optics Gonioscopy. The advances presented allow for fast, high-resolution 3D imaging of the human ICA and is suitable for clinical practice. The optimized gonioscopic OCT imaging will allow studying structural changes of the TM with age and disease, as well as medical and surgical treatments aimed at lowering IOP.

2. Methods

2.1. Custom goniolens optical design

The goniolens used in our pilot study on OCT gonioscopy [18,19] was modeled using Zemax Optic Studio ray tracing software. This initial design used a stock N-BK7 plano-convex spherical lens (22 mm focal length) placed on the anterior surface of a commercial single-mirrored goniolens at 59° built from PMMA (OSMG; Ocular Instruments Inc., Bellevue, WA). While the current study uses a smaller pupil, the lens was modeled for a 6.4 mm beam to be used with

multiple imaging devices, including adaptive optics systems which require large pupil sizes, at 780 nm and can provide an Airy disk radius of as little as 2.2 μm and an RMS radius of 42.89 μm .

The pilot design [18] had poor performance (Fig. 1, column 1), thus we used a multi-step approach to improve the optical performance. First, the spherical lens was replaced by an aspheric lens of the same glass type. This reduced the spherical aberration which halved the RMS radius of the imaging spot (Fig. 1, column 2). The main aberration source in this first iteration was the interface between the N-BK7 glass of the plano-convex lens and the anterior surface of the goniolens body. Thus, we next replaced the singlet lens with an N-BK7 air-spaced doublet such that the anterior lens is an aspheric bi-convex lens, and the posterior lens is a plano-convex spherical lens with its curvature matching the focal length of the first element, guiding light into the goniolens body (Fig. 1, column 3). This again reduced the RMS radius. The main remaining aberration is field dependent oblique astigmatism rising from light propagating at high angles through the curved interface between the PMMA ($n_d = 1.4918$) and the gonioscopic fluid ($n_d = 1.337$), cornea ($n_d = 1.377$) and aqueous ($n_d = 1.337$) respectively. Eliminating this aberration source required matching the refractive index of the goniolens body to that of the cornea. We modeled a body made of MgF_2 ($n_d = 1.3777$) which resulted in predicted diffraction limited performance with an RMS radius of 1.650 μm (Fig. 1, column 4).

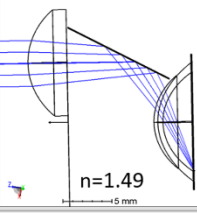
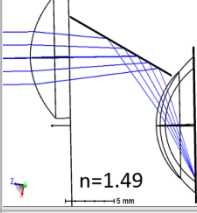
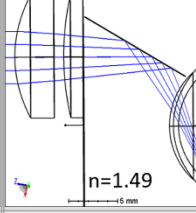
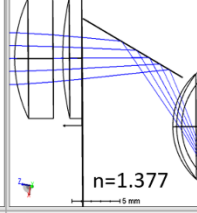
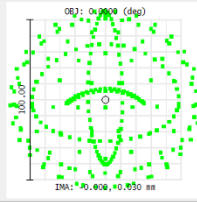
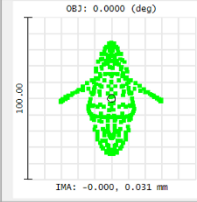
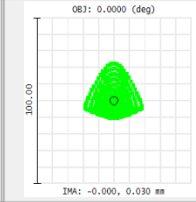
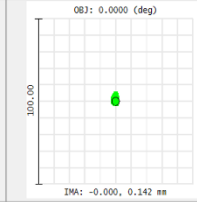
	Spherical (PMMA)	Aspherical (PMMA)	Air-Spaced (PMMA)	Air-Spaced (MgF_2)
Design				
Spot Diagram				
Airy radius	2.209 μm	2.31 μm	2.521 μm	2.405 μm
RMS radius	42.895 μm	21.064 μm	12.252 μm	1.650 μm
GEO radius	63.169 μm	34.475 μm	22.288 μm	4.399 μm

Fig. 1. Schematic table of design changes and performance of the goniolens modeled using Zemax Optic Studio optical design software for a 6.4 mm incident beam. Ray tracing of the design for each sequential step for improvement is shown in row 1. Performance after each sequential change is described by the spot diagram at the image plane, shown in row 2, the theoretically calculated Airy radius in row 3 and the modeled Root Mean Square (RMS) and geometric radii in rows 4 and 5.

The final goniolens design incorporates two interior mirrors at 59 and 63 degrees respectively and located on opposite sides of the goniolens. The use of the two angles allows for individual variation of anterior chamber depths between subjects, with the 63° mirror for deeper anterior chambers and the 59° for shallower anterior chambers. The air-spaced doublets were optimized for each case separately, varying the anterior and posterior curvatures and conic of the first element, the curvature of the anterior surface of the second element, and the spacing between the elements. Diffraction limited performance was obtained for both angled mirrors using a 6.4 mm

beam. The gonioscopic lens was designed with a 11.5 mm interior body length to accommodate for the short working distance of many OCT devices (~ 2.5 cm), and still allow the exit pupil of the imaging system to be placed on the goniolens mirror. This placement facilitates beam steering across the eye without vignetting at the mirrors. Finally, the customized focusing doublet lenses were substituted for stock lenses to reduce cost with minimal optical consequences. The final design can be seen in Fig. 2. The focusing air-spaced doublet for the 59° mirror consisted of a Thorlabs achromat of 30 mm focal length (AC127-030-B) and a plano-convex $f = 75$ mm lens (LA4327-B). For the 63° mirror, an Edmund Optics 40 mm focal length achromatic lens (#45-796) and a Thorlabs 50 mm focal length plano-convex lens (LA1213-B) were used.

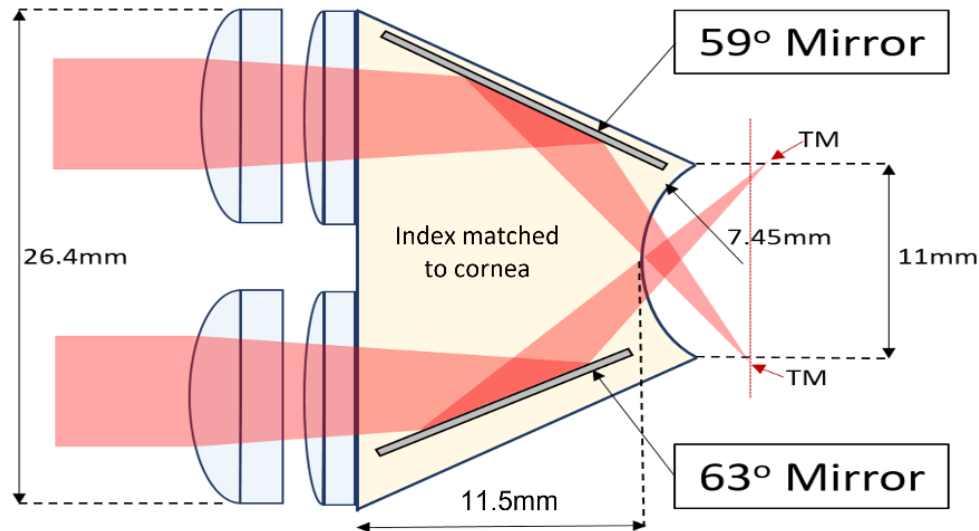


Fig. 2. Schematic of new two-mirror gonioscopic lens design optically optimized for high-resolution imaging. The body of the gonioscopic lens is index matched to the cornea to reduce aberrations. Optimized air-spaced doublets for each mirror are used to focus light at the TM.

For the Heidelberg Spectralis commercial OCT used in this study, the 2.5 mm pupil obtains diffraction-limited performance of the gonioscopic lens throughout a scan area of $1 \times 1 \text{ mm}^2$ at the image plane for both the 59° and the 63° mirrors. In the following section two fabrication processes are described including a MgF_2 body and an index matched fluid body. Diffraction-limited performance was obtained in both cases, as shown in Fig. 3 for the latter.

2.2. Fabrication of the custom designed gonioscopic lens

The final design shown in Fig. 2 was fabricated by two distinct processes.

- The first version was professionally custom manufactured by the Centro de Investigaciones Ópticas A. C. (CIO), León, Mexico. The main body of the gonioscopic lens was made from MgF_2 with the optical axis of the crystal aligned with the optical axis of the incident light. The flats for the mirrors were cut out from the main body to a surface flatness of $\lambda/4$. The mirror surfaces were coated with silver and covered with the slabs that had been removed to reconstruct the full posterior surface of the gonioscopic lens curved to couple to the cornea, as can be seen in Fig. 4(A). The edge of the posterior concave surface was beveled for safety and comfort when placed on the eye. This surface, and the exterior conic surface, were coated with 35 nm of SiO_2 to ensure inertness. The gonioscopic lens body was fitted with a 30 mm diameter blackened metal ring with apertures to fit the focusing lenses. The second elements of the air-spaced doublets for either mirror were glued to the anterior surface

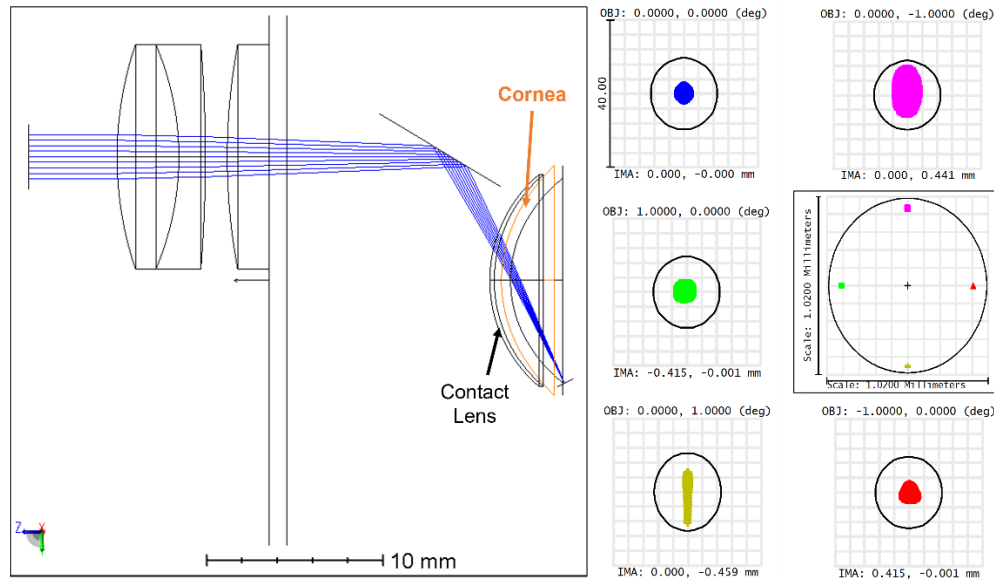


Fig. 3. Optical performance of the index matched fluid filled goniolens design, for the 59° mirror, over a 1 mm^2 field at the image plane. Left: Optical layout and ray tracing of the goniolens design for the center field. Right: Spot diagrams at the different field locations, as indicated in the footprint diagram in the black box. Airy radius is $9.349 \mu\text{m}$ as indicated by the black circle in each spot diagram. RMS radii for the 5 field locations are $1.352 \mu\text{m}$ (0, 0), $1.578 \mu\text{m}$ (1, 0), $3.701 \mu\text{m}$ (0, 1), $3.624 \mu\text{m}$ (0, -1) and $1.578 \mu\text{m}$ (-1, 0).

of the goniolens body with NOA 61 Norland ($n_d = 1.56$), centered over their respective mirrors. The first elements of the air-spaced doublets were placed with a spacer ring and held in place with a retaining ring.

- The second version was redesigned as a 3D printed shell for the goniolens body using SolidWorks (Dassault Systemes SolidWorks Corporation, Waltham, Massachusetts, USA) (as seen in Fig. 4(B) left) and filled with a fluid that is index-matched to that of the cornea. The shell was printed either with ECO-ABS black plastic using a commercial 3D printer (Dremel 3D45, Bosch Power Tool B. V., 3PI Tech Solutions, Rosemont, Illinois, USA) or with 420i - 420 Stainless Steel/Bronze by metal binder jetting and tumble polished, outsourced to Xometry (North Bethesda, Maryland, USA). The interior was painted with ultra-black water-based acrylic paint to absorb up to 99.4% of visible-light (Musou Black, KOYO Orient Japan Co., Ageo, Saitama, Japan), and protect the body from any interaction with the index-matched fluid. The posterior concave surface of the goniolens was composed of a 12 mm diameter, 0 diopter clinical contact lens (ABB Optical Group LLC., Coral Springs, Florida, USA) made of PPO2 with a base curve of 7.85 mm and a thickness of 0.3 mm. The contact lens was glued to the goniolens shell along the edge using Norland NOA 68 ($n_d = 1.54$). Flat 9 mm diameter and 1 mm thickness protected aluminum mirrors with a surface flatness peak-to-valley of $4-6\lambda$ (Edmund Optics #46-647) were glued to the flat surfaces of the shell at 59° and 63° respectively. Several index-matched fluids were tested including Isopropyl alcohol 99+% purity ($n_d = 1.3772$), n-Heptane (Pure Grade UN1206) ($n_d = 1.3855$ at 25°C), sucrose 30% ($n_d = 1.3812$) [31], and glycerol 35.6% ($n_d = 1.377$) [32], as is explained further in section 3. The goniolens shell was fitted and glued to a Thorlabs 30 mm diameter lens tube, which held a N-BK7 glass NIR I-coated window as the anterior surface of the goniolens body (Edmund Optics #23-430). The goniolens

shell was overfilled with the index-matched fluid, then sealed with a ring gasket and the glass window, avoiding air-bubbles and leakage. Both elements were held in place with a retaining ring. The plano-convex elements of the air-spaced doublets and aluminum support tubes were glued to the glass window with Norland NOA 61 ($n_d = 1.56$). Either tube held the corresponding air-spaced doublets, spacer rings, and retaining rings. A picture of the fabricated and mounted 3D printed goniolens with only the 63° angled mirror focusing lenses can be seen in Fig. 4(B) on the right. A full step-by-step description of this fabrication process can be found in [Supplement 1](#), as well as the SolidWorks model to print the 3D body part in [Code 1](#) [33].

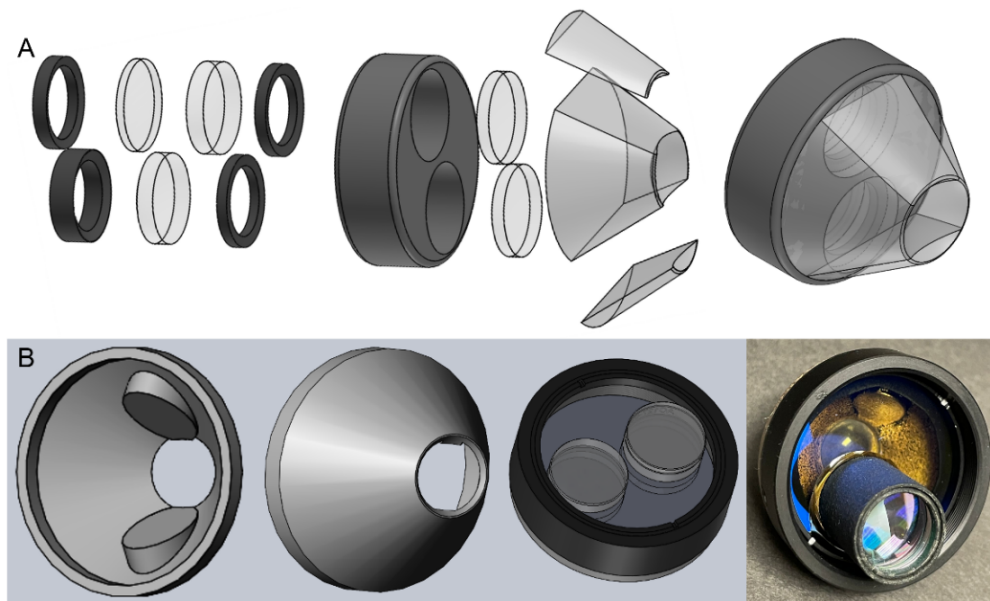


Fig. 4. A) Exploded view of the MgF_2 goniolens manufacturing process showing each one of its parts separately on the left and the fully assembled goniolens on the right. B) Design of the 3D printed goniolens shell (first and second image) and fully assembled model of the goniolens (third image), and picture, right, of a fabricated 3D metal printed goniolens lens (not blackened to show interior) with the mounted air-spaced doublet focusing lens for the 63° mirror.

2.3. Gonioscopic OCT

A commercial OCT device (Heidelberg Spectralis OCT2) was used to obtain gonioscopic OCT images. The goniolens was first placed on the subject's eye after its posterior surface was coated with a thick layer of gonioscopic fluid Lumecare Carbomer (Medicom Health Ltd., 7-12 Tavistock Square, Kings Cross, London, UK). As described previously [18], the goniolens was placed on the eye by a clinician aided with a 3D adjustable mount fixed to the head mount of the OCT imaging device for stability. The goniolens was aimed at the inferior-temporal sector of the ICA, with the scanning mirrors of the OCT conjugate to the goniolens mirror being used. All gonioscopic OCT imaging was performed using the retinal imaging mode of the OCT device, and the scan location and orientation was adjusted using the Heidelberg Spectralis software. Volumetric OCT scans of maximum $15 \times 5^\circ$ with $11 \mu\text{m}$ spacing between b-scans were performed. At least 2 OCT volume scans were performed per subject, although some volume scans covered less than 5° if eye movement or alignment impeded the acquisition of the full set of b-scans.

B-scan orientation was chosen to be tangential to the ICA and iris, maximizing the visibility of fine layered structures in the TM. All images are presented as produced by the Heidelberg Spectralis software without any additional post-processing or image enhancement.

2.4. Transverse structural OCT images

Transverse structural enface images were obtained using the segmentation options available on the Heidelberg Spectralis software for volumetric OCT scans. Segmentation was performed manually on all b-scans within a volumetric OCT along the anterior chamber, just below the surface of the uveal meshwork of the TM. The transverse images were generated based on the segmented line and displaced by 30-65 μm in depth for each subject until the lamellar structures were most visible.

2.5. Subjects

All individuals imaged (Table 1) received an anterior eye exam, including gonioscopy with a slit lamp prior to imaging. The study protocol was approved by the Indiana University Institutional Review Board and adhered to the Declaration of Helsinki. The subjects for this study were 7 healthy adults (23-73 years old) with normal eye exam results and 20/20 or better best corrected visual acuity. Subjects were free to choose which eye they preferred for imaging and all subjects selected the right eye. Anterior segment OCT imaging was performed on all subjects using the Carl Zeiss Visante 1000 Anterior Segment OCT. Measurements are summarized in Table 1. The anterior chamber angle was measured using the angle measurement tool in the Visante software on a horizontal OCT -scan across the eye. Angles were measured from the apex of the ICA, limited by the TM-Cornea intersection and the most anterior point of the iris folds that could block incident light. This ensures the measurement of the smallest angle at which light from the goniolens can reach the ICA apex. The nasal and temporal angles were measured and averaged. The central corneal thickness, anterior chamber width (TM-to-TM) and depth (measured from the posterior surface of the central cornea to the intersections with the width line at the center of the pupil) were measured with the Anterior Chamber caliper tool of the device's software.

Table 1. Subject data imaged with OCT gonioscopy including anterior chamber measurements measured with a Carl Zeiss Visante 1000 Anterior Segment OCT.

Subject	Age	Sex	Average Angle [deg]	Anterior Chamber Width [mm]	Anterior Chamber Depth [mm]	Central Corneal Thickness [μm]	Gonio Mirror Angle ($^{\circ}$)	Notes
S1	32	F	31.40	11.83	3.06	590	59	-
S2	37	F	27.35	12.57	3.37	560	59	-
S3	73	M	43.50	11.75	3.35	600	59	Cataract surgery
S4	30	F	34.35	11.78	3.21	510	63	-
S5	23	F	22.95	12.31	3.25	490	59	-
S6	28	M	38.00	12.16	3.29	500	59	-
S7	50	M	42.15	11.15	3.26	560	59	-

For gonioscopic OCT imaging, the eye was anesthetized with 1 drop of Proparacaine Hydrochloride USP 0.5% before starting the imaging session and approximately 15 minutes thereafter. Total gonioscopy imaging time was less than 30 minutes broken into several shorter intervals.

2.6. Calibration

A commercial model eye (SimulEye SLT, InsEYE LLC., Westlake Village California, USA) was modified to calibrate and test the resolution of the custom manufactured gonioscopes. Three test targets with known sizes were inserted at the location of the TM in the model eye: 1) A 5-0 Prolene blue monofilament suture (AD Surgical, Sunnyvale, CA, USA) of 0.13 mm diameter; 2) a glass microtube (AAAdvance Instruments, Stony Brook, New York, USA) of 0.3 mm outer diameter and 0.2 mm inner diameter; and 3) a USAF-1951T-22-P-M resolution test chart printed on photographic film (Applied Imaging Inc., Rochester, New York, USA). The model eye was then filled with gonioscopic fluid and sealed onto a glass coverslip. The model eye targets were imaged using both newly fabricated gonioscopes and the modified PMMA commercial gonioscopes with the Spectralis OCT device.

3. Results

3.1. Calibration of the OCT gonioscopic images with the custom gonioscopes

There are two measurements that require calibration. The first is the relation between actual distances within the anterior segment and the Heidelberg reported distances, and the second is the in situ optical (lateral) resolution of the combined OCT/Gonioscope system. To determine the spatial relations 5-0 Prolene blue monofilament suture (AD Surgical, Sunnyvale, CA, USA) was used. This suture has a 0.13 mm diameter and was measured in the model eye to be 107.6 μm in the horizontal direction and 180.4 μm in the vertical direction as an average of 6 measurements, providing a 1.2 lateral scale factor and a 0.721 axial scale factor between the real object size and that measured by the Spectralis software caliper tool. A similar result was obtained with the capillary tube achieving a 1.19 lateral scaling factor. Due to the geometry of the capillary tube, the curved glass wall created a “lensing” effect, deeming the axial measurements inaccurate.

The optical resolution of the OCT gonioscopic system was calculated by imaging a USAF target using the OCT system, and then extracting the transverse enface image (Fig. 5). The 3D printed gonioscope at 59° and 63° achieved resolutions of 40.32 cy/mm and 45.25 cy/mm, respectively. The contrast of the highest resolvable USAF bars was 26.8%. Similar results were obtained with the MgF₂ gonioscope at 45.25 cy/mm for either angled mirror. Both newly designed gonioscopes are an improvement over the 35.92 cy/mm of the modified PMMA commercial gonioscopes.

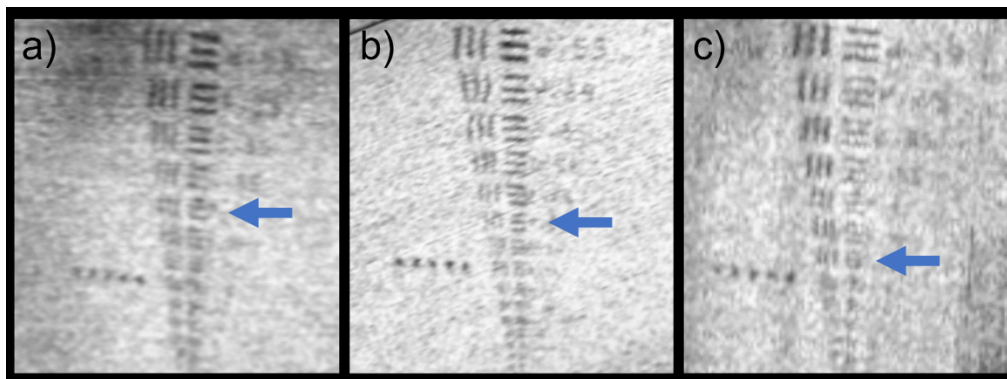


Fig. 5. Gonioscopic OCT enface images of a USAF target placed in a model eye at the iridocorneal angle with a) the modified clinical gonioscope providing a resolution of 35.92 cy/mm, and the 3D printed gonioscope b) at 59° providing a resolution of 40.32 cy/mm, and c) at 63° with a resolution of 45.25 cy/mm. Target is left-right inverted due to the reflection at the gonioscope mirror. Blue arrows indicate the achievable resolution.

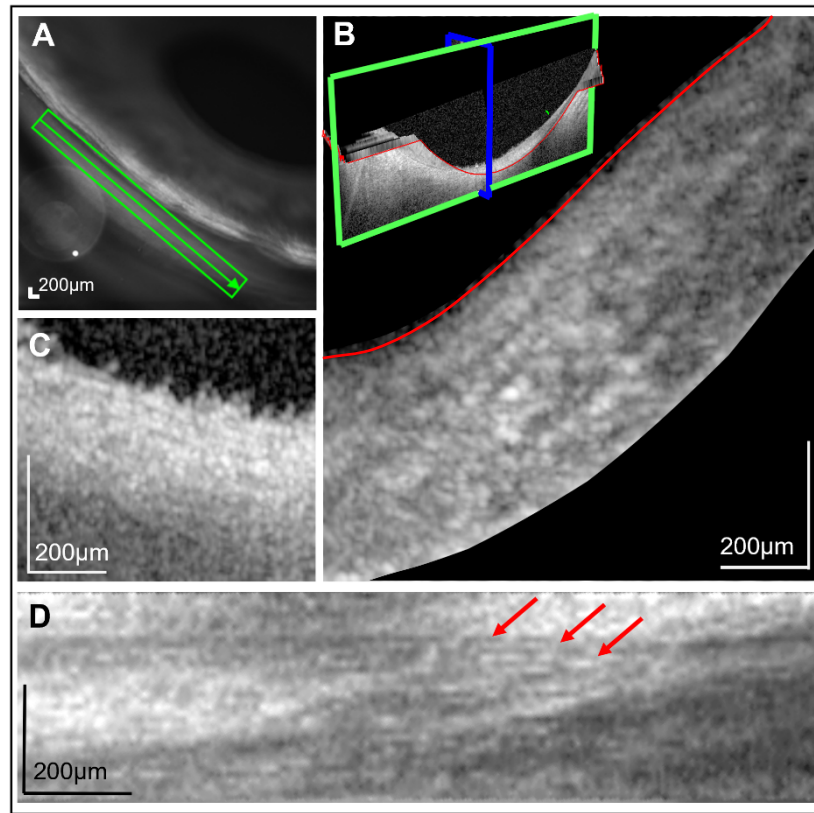


Fig. 6. Images of S1 with OCT gonioscopy and the MgF_2 custom goniolens using the 59° mirror aimed at the superior-nasal angle. A) Cropped Scanning Laser Ophthalmoscope image acquired by the OCT device at the start of the OCT scan, indicating the location and size of the OCT volume with a green square and a green arrow indicating the location and direction of a b-scan. B) Cropped gonioscopic b-scan of the TM. The image overlay indicates the direction of the a-scans in blue and the b-scans in green. The segmentation along the interface of the anterior chamber and the TM is shown in red on the image and the 3D overlay. Segmentation is used to construct the transverse enface image. C) Cropped gonioscopic b-scan focusing on the layer-like structures observed in the TM. D) Constructed enface image from the segmented OCT volume (as seen by looking down on the red line) focused on the same area seen in panel B). Red arrows indicate lamellar structures within the TM.

3.2. MgF_2 goniolens

Gonioscopic OCT images of the human ICA obtained with the MgF_2 goniolens for S1 are shown in Fig. 6. Due to the birefringent nature of the MgF_2 , the goniolens body was manufactured such that the axis of the crystal coincided with the principal optical axis. However, the effect of the birefringence caused by light passing through the crystal at an angle to its optical axis after reflecting off the goniolens mirror resulted in an image doubling (Fig. 6(A)). Gonioscopic images with the MgF_2 lens were optically excellent, but due to the birefringence, we only imaged two eyes (S1 and S3). Separation between the two images was sufficient to use the non-overlapping sections of the b-scans for analysis and segmentation. Cellular structures within the TM are observed in the b-scans for both subjects and an example is shown in Fig. 6(B)). Fine

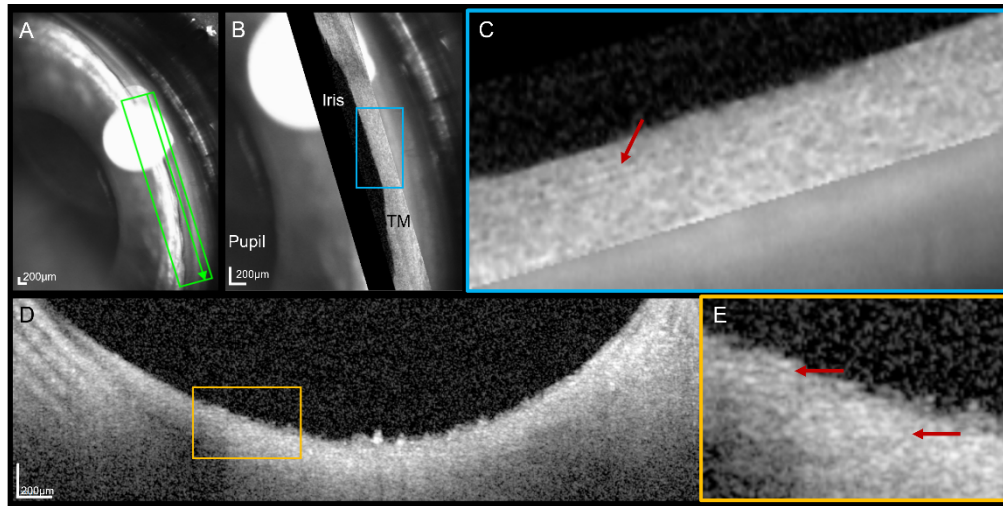


Fig. 7. Gonioscopic OCT images with the 3D printed goniolens for subject 1 at the inferior-temporal angle. A) SLO image through the goniolens. The green box indicates the location and size of the OCT volume, and the green arrow indicates the orientation of the b-scan. B) SLO image overlapped with the constructed enface image at a depth of 13 μm from the anterior TM. Blue box indicates the location of the expanded and cropped enface image seen in panel C). D) Gonioscopic OCT b-scan oriented tangential to the iris and ICA as seen by the green arrow in A). Yellow box indicates the region that has been expanded in panel E). Red arrows point at lamellar structures.

lamellar-like structures are observed in several b-scans for S1 (Fig. 6(C)). After segmentation, lamellar structures are also observed in the enface image (Fig. 6(D)).

3.3. 3D printed goniolens

As mentioned in section 2.2, four fluids index matched to the cornea were tested: n-Heptane (Pure Grade UN1206) ($n_d = 1.3855$ at 25°C), Isopropyl alcohol 99+% purity ($n_d = 1.3772$), and both sucrose and water, and glycerol and water solutions respectively. Isopropyl was a suitable option, with a close to 100% transmittance at 870 nm [34] but is toxic to the eye, and thus its use was avoided. Heptane is a safer option for the eye, but due to its low viscosity, was difficult to hermetically seal. A sucrose solution at 30% concentration was made to achieve a refractive index of $n_d = 1.3812$ [31]. The concentration of the glycerol solution to achieve a refractive index of 1.377 at 870 nm was 35.62% as calculated by Eq. (5) in [32] and compared to the result using the Lorentz-Lorenz relation for predicting the refractive index of binary mixtures of liquids [35], where $n_{\text{pure_glycerol}} = 1.4652$ and $n_{\text{water}} = 1.3282$ at 870 nm. Both the sucrose and glycerol solutions have a $\sim 90\%$ transmittance at 870nm [36–38]. The solutions were degassed to reduce bubbles that often appeared over time by heating using a magnetic stirrer hot plate or by using a degassing vacuum pump.

The ECO-ABS 3D printed shell was printed at 100% fill factor. However, slow fluid loss occurred, presumably due to diffusion through the layers of the print, and thus, this material was deemed unsuitable. The metal 3D printed shell did not have this problem and retained fluid without loss over periods of months. This was used for patient imaging.

An interface gasket was needed between the window material and the fluid filling the body of the lens. Several materials were tested including nitrile rubber, silicone rubber and 60A neoprene rubber sheets, as well as liquid silicone RTV gasket maker. For the rubber options, rings were

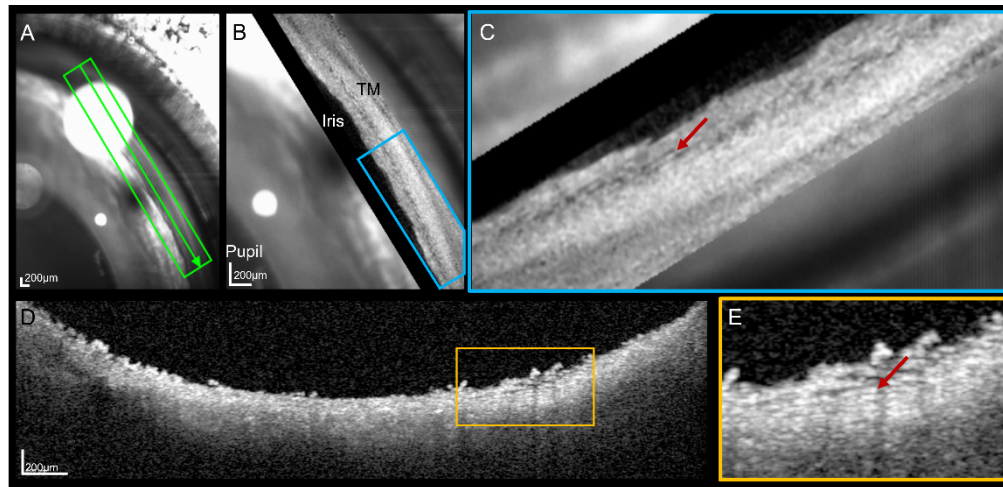


Fig. 8. Gonioscopic OCT images with the 3D printed gonioscopes for subject 4. A) SLO image through the gonioscopes. The green box indicates the location and size of the OCT volume, and the green arrow indicates the orientation of the b-scan. B) SLO image overlapped with the constructed enface image at a depth of 13 μm from the anterior TM. Blue box indicates the location of the expanded and cropped enface image seen in panel C). D) Gonioscopic OCT b-scan oriented tangential to the iris and ICA as seen by the green arrow in A). Yellow box indicates the region that has been expanded in panel E). Red arrows point at lamellar structures.

cut to 31 mm outer diameter and 26 mm inner diameter. The Nitrile and silicon options would absorb some of the fluids (alcohol and heptane) expanding their dimensions over time and causing leakage. The liquid silicon gasket was unsuitable as it did not dry adequately when in contact with the fluid. The neoprene rubber did not react with any of the tested fluids, it created an airtight seal, and was used for imaging.

Gonioscopic OCT images of the TM were captured using the 3D printed gonioscopes filled with 35.62% glycerol solution. Results for subjects 1 and 4 can be seen in Fig. 7 and Fig. 8 respectively. Panel A shows the SLO image of the inferior-temporal angle of the right eye indicating with a green box the location where the OCT volume was acquired, and the exact location of the b-scan is shown in panel D with a green arrow. Panel B shows the SLO image from A overlapped with the segmented enface image obtained from the OCT volume. The blue box indicates the region that has been enlarged in panel C. The yellow box in D has been enlarged in panel E. Red arrows point to fine lamellar-like structures observed in both the b-scan (panel E) and enface image (panel C).

It can be observed that S4 has more hypo-reflective sections within the TM (Fig. 8), suggesting larger spacing between the lamellar-like hyper-reflective structures or a lower matrix density surrounding the lamellae. This is observed throughout the entirety of the OCT volume.

4. Discussion

A novel gonioscope was designed and optically optimized to improve the optical resolution of imaging the human trabecular meshwork. The gonioscope was first modeled using ray tracing software, and two different implementations were created and tested. Based on the modeling, diffraction-limited performance is limited in the standard gonioscope designs by two main aspects. First, the inefficient coupling of light into the body of the gonioscope, creating aberrations at the interface between the singlet focusing lens and the PMMA body. Second, while the index

difference between the PMMA and cornea is less than in air, this interface is traversed at a high and field-dependent angle. By refractive index matching the goniolens body to that of the human cornea and optimizing the focusing lenses to couple light into the goniolens with an air-spaced doublet, aberrations could be greatly reduced. For a 2.5 mm incident beam, corresponding to that of the Heidelberg Spectralis, diffraction limited performance is obtained over a field of 1 mm^2 at the image plane. Given the geometry of the goniolens and its position relative to the cornea and the ICA, for larger scan areas, the performance progressively decreases as the location of the scanning beam nears the corneal edge of the ICA and the iris, whilst along the ICA moving coronally to the eye and the TM, the performance is maintained. This is due to the higher angle at which the rays are incident on the goniolens-cornea interface as can be observed in Fig. 3, where superior (toward the iris) and inferior (towards the cornea) fields, although diffraction-limited, have a larger spot diagram.

Implementation of the design using both a MgF_2 crystal body and an index matched fluid body was successful. The prototype using MgF_2 provided excellent optical quality, achieving an optical resolution of 45.25 cy/mm equivalent to $11.05 \text{ }\mu\text{m}$ per line on the USAF target. This design, however, suffered from doubling of the image by birefringence due to light traveling through the material off the optical axis of the crystal after reflecting from the interior goniolens mirror. To reduce cost ($> \$5,000$ for the MgF_2 lens), fragility, and avoid the effects of birefringence, the final design of the lens was fabricated by 3D printing a metal goniolens body shell and filling it with an optically transmissive fluid (glycerol solution) to achieve a 1.377 refractive index at 870nm [35,36]. The optical resolution matched that of the manufactured MgF_2 goniolens (40.32 cy/mm and 45.25 cy/mm for the 59° and 63° mirrors, respectively) and achieved a 2-element improvement on the USAF chart in comparison with the modified PMMA commercial goniolens. Slightly higher resolution is observed in the horizontal lines of the target in Fig. 5(c) and in the vertical lines in Fig. 5(b). This is due to the OCT b-scan orientation and the anisotropic sampling of pixels, with higher sampling along the b-scan. Slight misalignment between the b-scan will show a larger effect on narrow features (lines oriented transversely to the scan) versus larger features (line oriented in the same direction as the scan). The highest achievable contrast at the image plane was measured using the “finder squares” (5 black marker squares for density measurement on the USAF chart in Fig. 5). Then, the relative contrast of the highest resolution USAF bars (40.32 cy/mm and 45.25 cy/mm for the 59° and 63° mirrors) is 53.6% and 34.81%. On the other hand, a Modulation Transfer Function (MTF) graph plots the percentage of transferred contrast versus the frequency (cycles/mm) of the lines [39]. Therefore, the resolution values achieved with the USAF target have been compared to the Huygens MTF function in Zemax for 1 mm^2 field and corrected for 870 nm wavelength. In this case, the contrast values measured equate a spatial frequency on the Huygens MTF of 49 cy/mm and 64.5 cy/mm spatial frequency, respectively. Some discrepancy between the theoretical MTF and the real-world performance of the optical system is expected due to manufacturing tolerances and modeling limitations.

Hereafter, we describe some limitations of this study and discuss possible improvements to overcome them. First, the model eye is designed for selective laser trabeculoplasty training, and the refractive index of the model eye’s cornea differs from both the Zemax modeled cornea and that of the real eye. This difference is expected to produce a conservative estimate of our resolution compared to the better index matching *in vivo*, suggesting that our lens can achieve a higher resolution than 45.25 cy/mm. In addition, the OCT imaging beam has a bandwidth of $\sim 40 \text{ nm}$, hence slight differences of the refractive index occur across the spectrum.

Second, the modeling of the goniolens does not include the OCT optical system, hence the actual measurements are impacted by both the OCT noise, requiring higher contrasts, and the scan sampling. The goniolens mirror flatness has proven to not be a critical feature as similar resolution is obtained with the MgF_2 lens using a $\lambda/4$ quality mirror versus a $4\text{--}6\lambda$ quality for

the 3D printed design. However, improvement in the signal-to-noise ratio can be gained by using silver coated mirrors ($\sim 98\%$ reflectance at 870 nm) versus aluminum ($\sim 87\%$ reflectance) [40], which was originally chosen as silver mirrors were not commercially available. Higher scan sampling can be achieved using the OCTA imaging modality on the Heidelberg Spectralis down to 6 μm between b-scans, although slight movements of the eye impede rapid capture and alignment of the b-scans, limiting the acquisition. Additionally, manual segmentation, which is lengthy and tedious, is currently required as the automated software is mainly optimized for retinal OCT images. Custom segmentation software would highly improve post-processing time.

Third, the index matched fluid is a two-component solution (glycerin and water). This mixture has proven to maintain its properties over several weeks, but the solution may dissociate over longer periods of time. We proposed a more well-defined alternative using isopropyl alcohol ($n_{870\text{nm}} = 1.3778$), as a single substance liquid with excellent transmission ($\sim 100\%$) [34] and with minimum air bubble issues. The disadvantage for isopropyl alcohol is that while no visible leaks or deterioration of the contact lens has been observed over time, isopropyl alcohol is toxic to the human corneal epithelium, and any inadvertent liquid loss would be dangerous to the eye. As a result, we have not used this. However, given the robustness of the current lens, a more extensive study of possible leaks can be carried out. Alternatively, fabrication of a more complex lens with a single continuous surface from the frustrum to the corneal surface may be possible.

Finally, the pupil of the Heidelberg Spectralis OCT device is fixed at 2.5 mm which limits the Airy disk radius to 9.349 μm . To further improve the optical performance, a custom or commercial OCT device with a pupil double its size will have a 4.621 μm Airy radius while maintaining diffraction-limited performance for the current gonioscopic design. However, the major limitation is that while we improved resolution by reducing the aberrations arising from the curved surfaces coupled to the cornea, small changes in the refractive indices at the interfaces between the gonioscopic body fluid, the contact lens, the layer of gonioscopic gel and the cornea with incident light at high angles still contribute to the overall aberrations and optical performance of the system, and these limitations would intrude with larger pupil sizes.

In summary, we have provided a redesigned gonioscopic lens which allows high resolution imaging using a commercial OCT system designed for retinal imaging. Using this combination, we have been able to demonstrate imaging of the lamellar-like structures known to be present in the TM, but not observable in living humans using other techniques. The approach to fabrication is robust and the lens is easily assembled, and clinically suitable, as it uses a commercial contact lens to couple to the subject's cornea. This improved approach should enhance future quantification and measurement of the TM layers *in vivo*, as well as allow a better understanding of the changes to the iridocorneal angle that occur with age and changes in IOP. Increasing signal-to-noise ratio using a custom system can improve contrast between the collagenous corneal beams and the surrounding glycosaminoglycan matrix, as well as visualizing narrowing or collapsing of the intertrabecular beam spacing. These are important pathological findings in glaucoma.

5. Conclusions

A commercial Heidelberg Spectralis OCT device has successfully been used to image the human trabecular meshwork with sufficient resolution to depict fine structural features. The gonioscopic lens has been redesigned to improve its optical resolution by index matching its refractive index to that of the human cornea. The new design includes two gonioscopic mirrors at 59 and 63 degrees and corresponding air-spaced doublet focusing lenses optimized for each mirror. The design has been fabricated by 3D printing a metal gonioscopic body, with a commercial contact lens at its posterior surface, and filled with a glycerol solution index matched to the cornea. Enface gonioscopic OCT images of the human TM are captured with an optical resolution of 45.25 cy/mm equating to 11.05 μm lines. This high-resolution gonioscopic OCT allows imaging of

fine collagenous structures within the TM that are not resolvable with commercially available systems using a clinically feasible approach.

Funding. BrightFocus Foundation (G2022001F); National Center for Advancing Translational Sciences (TL1TR002531); National Eye Institute (1R0EY024315); Alcon Research Institute.

Disclosures. The authors declare no conflicts of interest.

Data availability. Data underlying the results presented in this paper are not publicly available at this time but may be obtained from the authors upon reasonable request.

Supplemental document. See [Supplement 1](#) for supporting content.

References

1. P. Foster, R. Buhrmann, H. Quigley, and G. Johnson, "The definition and classification of glaucoma in prevalence surveys," *Br J Ophthalmol* **86**(2), 238–242 (2002).
2. H. Taylor and J. Keefe, "World blindness: a 21st century perspective," *Br J Ophthalmol* **85**(3), 261–266 (2001).
3. H. Kahn, H. Leibowitz, J. Ganley, M. Kini, T. Colton, R. Nickerson, and T. Dawber, "The Framingham Eye Study. I. Outline and major prevalence findings," *Am J Epidemiol* **106**(1), 17–32 (1977).
4. M. Kini, H. Leibowitz, T. Colton, R. Nickerson, J. Ganley, and T. Dawber, "Prevalence of senile cataract, diabetic retinopathy, senile macular degeneration, and open-angle glaucoma in the Framingham eye study," *Am J Ophthalmol* **85**(1), 28–34 (1978).
5. B. Davis, L. Crawley, M. Pahlitzsch, F. Javaid, and M. Cordeiro, "Glaucoma: the retina and beyond," *Acta Neuropathol* **132**(6), 807–826 (2016).
6. M. Shields, "Normal-tension glaucoma: is it different from primary open-angle glaucoma?" *Curr Opin Ophthalmol* **19**(2), 85–88 (2008).
7. P. G. D. Spry, J. M. Sparrow, J. P. Diamond, and H. S. Harris, "Risk factors for progressive visual field loss in primary open angle glaucoma," *Eye* **19**(6), 643–651 (2005).
8. W. D. Stamer, S. T. Braakman, E. H. Zhou, C. R. Ethier, J. J. Fredberg, D. R. Overby, and M. Johnson, "Biomechanics of Schlemm's canal endothelium and intraocular pressure reduction," *Prog Retin Eye Res* **44**, 86–98 (2015).
9. D. R. Overby, J. Bertrand, M. Schicht, F. Paulsen, W. Daniel Stamer, and E. Lütjen-Drecoll, "The structure of the trabecular meshwork, its connections to the ciliary muscle, and the effect of pilocarpine on outflow facility in mice," *Invest. Ophthalmol. Vis. Sci.* **55**(6), 3727–3736 (2014).
10. E. Tamm, "The trabecular meshwork outflow pathways: structural and functional aspects," *Exp Eye Res* **88**(4), 648–655 (2009).
11. T. Carreon, E. van der Merwe, R. Fellman, M. Johnstone, and S. Bhattacharya, "Aqueous outflow - A continuum from trabecular meshwork to episcleral veins," *Prog Retin Eye Res* **57**, 108–133 (2017).
12. T. S. Acott and M. J. Kelley, "Extracellular matrix in the trabecular meshwork," *Exp Eye Res* **86**(4), 543–561 (2008).
13. S. C. Saccà, S. Gandolfi, A. Bagnis, G. Manni, G. Damonte, C. Traverso, and A. Izzotti, "The outflow pathway: a tissue with morphological and functional unity," *J. Cell. Physiol.* **231**(9), 1876–1893 (2016).
14. O. Tektas and E. Lütjen-Drecoll, "Structural changes of the trabecular meshwork in different kinds of glaucoma," *Exp Eye Res* **88**(4), 769–775 (2009).
15. J. Ueda and B. Yue, "Distribution of myocilin and extracellular matrix components in the corneoscleral meshwork of human eyes," *Invest. Ophthalmol. Vis. Sci.* **44**(11), 4772–4779 (2003).
16. J. Vranka, M. Kelley, T. Acott, and K. Keller, "Extracellular matrix in the trabecular meshwork: intraocular pressure regulation and dysregulation in glaucoma," *Exp Eye Res* **133**, 112–125 (2015).
17. C. Cavallotti, J. Feher, N. Pescosolido, and P. Sagnelli, "Glycosaminoglycans in human trabecular meshwork: age-related changes," *Ophthalmic Res* **36**(4), 211–217 (2004).
18. A. Carmichael-Martins, B. J. King, B. R. Walker, S. A. Burns, and T. J. Gast, "Characterization of the human iridocorneal angle in vivo using a custom design gonioscopy with OCT gonioscopy," *Biomed. Opt. Express* **13**(9), 4652–4667 (2022).
19. B. J. King, S. A. Burns, K. A. Sapoznik, T. Luo, and T. J. Gast, "High-resolution, adaptive optics imaging of the human trabecular meshwork in vivo," *Trans. Vis. Sci. Tech.* **8**(5), 5 (2019).
20. P. Li, T. Shen, M. Johnstone, and R. Wang, "Pulsatile motion of the trabecular meshwork in healthy human subjects quantified by phase-sensitive optical coherence tomography," *Biomed. Opt. Express* **4**(10), 2051 (2013).
21. Z. Chen, Y. Song, M. Li, W. Chen, S. Liu, Z. Cai, L. Chen, Y. Xiang, H. Zhang, and J. Whang, "Schlemm's canal and trabecular meshwork morphology in high myopia," *Ophthalmic Physiol Opt* **38**(3), 266–272 (2018).
22. E. Crowell, L. Baker, A. Chuang, R. Feldman, N. Bell, P. Chévez-Barrios, and L. Blieden, "Characterizing Anterior Segment OCT Angle Landmarks of the Trabecular Meshwork Complex," *Ophthalmology* **125**(7), 994–1002 (2018).
23. J. I. Fernández-Vigo, J. García-Feijóo, J. M. Martínez-de-la-Casa, J. García-Bella, and J. A. Fernández-Vigo, "Morphometry of the trabecular meshwork in vivo in a healthy population using fourier-domain optical coherence tomography," *Invest Ophthalmol Vis Sci* **56**(3), 1782–1788 (2015).
24. M. Sarunic, S. Asrani, and J. Izatt, "Imaging the ocular anterior segment with real-time, full-range Fourier-domain optical coherence tomography," *Arch. Ophthalmol.* **126**(4), 537–542 (2008).

25. Y. Yasuno, M. Yamanari, K. Kawana, M. Miura, S. Fukuda, S. Makita, S. Sakai, and T. Oshika, "Visibility of trabecular meshwork by standard and polarization-sensitive optical coherence tomography," *J. Biomed. Opt.* **15**(6), 061705 (2010).
26. M. Yoshikawa, T. Akagi, A. Uji, H. Nakanishi, T. Kameda, K. Suda, H. Ikeda, and A. Tsujikawa, "Pilot study assessing the structural changes in posttrabecular aqueous humor outflow pathway after trabecular meshwork surgery using swept-source optical coherence tomography," *PLoS One* **13**(6), e0199739 (2018).
27. X. Yao, B. Tan, Y. Ho, X. Liu, D. Wong, J. Chua, T. T. Wong, S. Perera, M. Ang, R. M. Werkmeister, and L. Schmetterer, "Full circumferential morphological analysis of Schlemm's canal in human eyes using megahertz swept source OCT," *Biomed. Opt. Express* **12**(7), 3865 (2021).
28. A. S. Huang, A. Belghith, A. Dastiridou, V. Chopra, L. M. Zangwill, and R. N. Weinreb, "Automated circumferential construction of first-order aqueous humor outflow pathways using spectral-domain optical coherence tomography," *J. Biomed. Opt.* **22**(6), 066010 (2017).
29. S. Luo, G. Holland, R. Khazaeinezhad, S. Bradford, R. Joshi, and T. Juhasz, "Iridocorneal angle imaging of a human donor eye by spectral-domain optical coherence tomography," *Sci. Rep.* **13**(1), 13861 (2023).
30. R. P. McNabb, P. Challa, A. N. Kuo, and J. A. Izatt, "Complete 360° circumferential gonioscopic optical coherence tomography imaging of the iridocorneal angle," *Biomed. Opt. Express* **6**(4), 1376 (2015).
31. "Refractive index of sucrose solutions.," <http://www.refractometer.pl/refraction-datasheet-sucrose>.
32. C. İde and K. Yüksel Aldoğan, "Experimental Investigation of Refractive Index Measurement of Common Solvents and Aqueous Solutions in the Infrared Wavelengths," *Balkan Journal of Electrical and Computer Engineering* **6**(3), 159–164 (2018).
33. A. Carmichael-Martin, T. J. Gast, B. J. King, B. Walker, M. Sobczak, and S. A. Burns, "Solidworks model of a new design gonioscopy lens body for 3D printing," figshare, 2018, <https://doi.org/10.6084/m9.figshare.23686491>.
34. F. S. Rocha, A. J. Gomes, C. N. Lunardi, S. Kaliaguine, and G. S. Patience, "Experimental methods in chemical engineering: Ultraviolet visible spectroscopy—UV-Vis," *Can. J. Chem. Eng.* **96**(12), 2512–2517 (2018).
35. J. V. Herráez and R. Belda, "Refractive indices, densities and excess molar volumes of monoalcohols + water," *J Solution Chem* **35**(9), 1315–1328 (2006).
36. O. A. Journal, K. Musa, and A. M. Hammadi, "Design and Fabrication of Evanescent Wave Fiber Optic Sensor," *Advances In Natural And Applied Sciences* **11**, 130–139 (2017).
37. P. Zaca-Morán, J. P. Padilla-Martínez, J. M. Pérez-Corte, J. A. Dávila-Pintle, J. G. Ortega-Mendoza, and N. Morales, "Etched optical fiber for measuring concentration and refractive index of sucrose solutions by evanescent waves," *Laser Phys.* **28**(11), 116002 (2018).
38. A. Al-Kahlout, D. Vieira, C. O. Avellaneda, E. R. Leite, M. A. Aegerter, and A. Pawlicka, "Gelatin-based protonic electrolyte for electrochromic windows," *Ionics* **16**(1), 13–19 (2010).
39. "Introduction to Modulation Transfer Function | Edmund Optics," <https://www.edmundoptics.com/knowledge-center/application-notes/optics/introduction-to-modulation-transfer-function/>.
40. J. M. Bennett and E. J. Ashley, "Infrared Reflectance and Emittance of Silver and Gold Evaporated in Ultrahigh Vacuum," *Appl. Opt.* **4**(2), 221 (1965).